

# Interpretation of in-air output ratio and its impact on Dose Calculation

Timothy C Zhu<sup>1</sup> and Anders Ahnesjö<sup>2,3</sup>

<sup>1</sup>Dept. of Radiation Oncology, University of Pennsylvania, Philadelphia, PA, <sup>2</sup>Nucletron Scandinavia AB, Uppsala, Sweden and <sup>3</sup>Dep. Rad. Phys. Umeå University, Umeå, Sweden

## I. Introduction

The concept of in-air output ratio ( $S_c$ ) was introduced to characterize how the incident photon fluence per monitor unit (or unit time for a Co-60 unit) varies with collimator settings.<sup>1,2</sup> This quantity is also called in-air output factor,<sup>3</sup> collimator-scatter factor,<sup>4</sup> and headscatter factor.<sup>5,6</sup> The latter two names were somewhat misleading since they emphasized a single component of the output ratio. We retained the symbol  $S_c$  because it has been widely used<sup>4</sup>. In the early 90s, the development of conformal radiotherapy based on 3D treatment planning motivated development of models and experimental procedures to quantify different components of the accelerator output. There are multiple factors shown to influence the in-air output ratio<sup>7</sup>, in particular, photons are scattered by structures in the accelerator head (head scatter), photons and electrons are backscattered into the monitor chamber (monitor backscatter), and at very small field sizes, a portion of the x-ray source is obscured by the collimators (source obscuring effect). Various sources of headscatter, the primary collimator, the flattening filter, the secondary collimators, the monitor chamber (and a wedge, if used), have been characterized. Several studies have measured the actual source distributions for the target as well as for the extended headscatter source at the flattening filter.<sup>8-10</sup> To separate the components of the in-air output ratio requires additional measurements. The availability of Monte Carlo simulation has provided a methodology to separate various components of the headscatter to interpret the measurement results, or validate analytical models.

The main problem in measuring the in-air output ratio concerns the design of the build-up cap, or miniphantom, to use together with a suitable detector. Ideally, the cap/phantom should provide full electron equilibrium as in water medium, without any photon scattering, and be small enough to be fully covered by the radiation beam. Hence, there has been much confusion regarding the measurement technique that has prevented the accurate and consistent determination of this quantity. Questions remain on the shape, dimension and material of the buildup cap/miniphantom, and on the type and size of the detector. Earlier designs of buildup caps were very thin, with a water-equivalent thickness of approximately 0.5 cm for use in Cobalt beams. They were fine for cobalt. At higher energies ( $E > 6$  MV), similar build-up caps or miniphantoms with longitudinal thickness equal to the depth of maximum dose of the incident photons are generally not suitable for measurement of  $S_c$  due to the presence of electron contamination.<sup>11</sup> The main problem with a miniphantom for photons of higher energies is that one may not find a size large enough to exclude the electrons from outside the miniphantom, yet small enough that scattered photons generated within the phantom can be completely ignored. Thus, a suitable compromise is needed that minimizes risk for large handling errors while not introducing significant systematic errors.

We will provide a comprehensive review of the current status including the clinical significance of the output ratio and the findings of existing theoretical and experimental investigations.

## II. Definition of in-air output ratio

In the following, we will need to distinguish different beam components, as outlined in Table 1..

The **in-air output ratio**,  $S_c$ , is defined as the ratio of primary collision kerma in-water,  $K_p$ , per monitor unit (M) between an arbitrary collimator setting and the reference collimator setting at the same location:

$$S_c \equiv \frac{K_p(c; z_{ref}) / M}{K_p(c_{ref}; z_{ref}) / M}, \quad (1)$$

where  $c$  is the collimator setting,  $c_{ref}$  is the collimator setting under reference condition, usually  $10 \times 10 \text{ cm}^2$ , and  $z_{ref}$  is the reference source-to-detector distance, usually  $z_{ref} = 100 \text{ cm}$ . Notice that the primary collision kerma excludes the scattered collision kerma generated in any surrounding phantom but includes all scattering that have occurred in the treatment head. Hence, the in-air output ratio is the ratio of the products of the energy absorption coefficient in-water and the output photon energy fluence, i.e.

$$S_c \equiv \frac{\int_{\text{Spectrum } c} (\mu_{en}(E) / \rho) \cdot e^{-\mu(E)d} \cdot \Psi_E(c; z_{ref}) / M \cdot dE}{\int_{\text{Spectrum } c_{ref}} (\mu_{en}(E) / \rho) \cdot e^{-\mu(E)d} \cdot \Psi_E(c_{ref}; z_{ref}) / M \cdot dE} \approx \frac{\Psi(c; z_{ref}) / M}{\Psi(c_{ref}; z_{ref}) / M}, \quad (2)$$

where  $(\mu_{en}/\rho)$  is the mass energy absorption coefficient for photon energy  $E$ ,  $d$  is the depth in miniphantom, and  $\Psi_E(c; z_{ref})$  and  $\Psi_E(c_{ref}; z_{ref})$  are the energy fluence spectra for beam  $c$  and  $c_{ref}$ , respectively.  $\Psi(c; z_{ref})$  and  $\Psi(c_{ref}; z_{ref})$  are the energy fluence for beam  $c$  and  $c_{ref}$ , respectively. Since the beam quality is approximately independent of collimation, it follows that  $S_c$  effectively measures the energy fluence output ratio. However, in situations when the beam quality is different from reference conditions (e.g. while using solid wedges), it has to be noticed that  $S_c$  as an estimator of the energy fluence ratio that is biased by the collision kerma and attenuation at measurement depth. Experimentally,  $S_c$  can be determined as the ionization ratio measured in a miniphantom with sufficient thickness to eliminate electron contamination. The lateral dimensions of the miniphantom must, besides outfiltering contaminant electrons, provide lateral electronic equilibrium at the detector while not contributing significant scatter. The material composition of the miniphantom must be carefully chosen as to not introduce significant medium based deviations from water kerma ratios due to spectral differences between beam  $c$  and  $c_{ref}$ . Details on the measurement are discussed later.

In cases with measurement made at an off-axis location  $(x, y)$ ,  $S_c$  defined in Eq. (2) can be expanded by measuring the primary collision kerma for both the nominator and denominator at the same location:

$$S_c \equiv \frac{K_p(c; x, y, z_{ref}) / M}{K_p(c_{ref}; x, y, z_{ref}) / M} \quad (3)$$

This definition avoids the introduction of off-axis variation of the direct fluence. A more general quantity is the **primary output function** for the incident photon beam,  $POF$ , defined as the ratio of primary collision kerma in-water per monitor unit for an arbitrary collimator setting and the primary collision kerma in-water per monitor unit for the open beam under reference condition:

$$POF \equiv \frac{K_p(c; x, y, z) / M}{K_{p,open}(c_{ref}; x_{ref}, y_{ref}, z_{ref}) / M}. \quad (4)$$

Notice that  $POF$  at the isocenter is identical to the in-air output ratio for the open beam but it will have different values at an arbitrary source-to-detector distance ( $z \neq 100 \text{ cm}$ ) since  $S_c$  is a ratio defined at a fixed  $z_{ref}$ . If a wedged beam is used,  $POF$  includes the transmission of the wedge filter as well.

### III. THE ROLE OF $S_c$ FOR MU CALCULATION

#### A. Factor based dose-to-dose ratio formalisms

Factor based methods are designed to arrive at the dose per monitor unit by using standardized dose ratio measurements. This is accomplished through multiplying dose ratio factors for a chain of geometries where the variables determining the irradiation geometry are varied one by one until the geometry of interest is linked back to the reference geometry:

$$\frac{D}{M}(caseA) = \frac{D/M_{caseA}}{D/M_{caseB}} \cdot \frac{D/M_{caseB}}{\dots} \cdot \frac{\dots}{D/M_{calib}} \cdot \frac{D}{M}(ref). \quad (5)$$

This equation is also called the identity equation. A systematic example of a dose-to-dose ratio formalism has been given in the ESTRO protocol<sup>1</sup>. The strength of the formalism lies in that the calculations are simple and based on measured data. Obviously, one strives for as few and general factors as possible, where some might be modelled instead of measured (e.g. the inverse square factor). As an example, the dose on the central-axis can be expressed as the result of three factors

$$\begin{aligned} D(z; s, d) / M &= \frac{D(z; s, d)}{D(z; s, d_{ref})} \cdot \frac{D(z; s, d_{ref})}{D(z; s_{ref}, d_{ref})} \cdot \frac{D(z; s_{ref}, d_{ref})}{D(z_{ref}; s_{ref}, d_{ref})} \cdot D(ref) / M \\ &= TPR(s, d) \cdot S_{cp}(s) \cdot INV(z) \cdot D(ref) / M, \end{aligned} \quad (6)$$

where  $TPR(s, d)$  is the tissue phantom ratio and  $INV(z)$  the inverse square law.  $D(ref)/M$  is the dose per monitor unit (cGy/MU) at the reference condition. We ignore the source-to-detector distance ( $z$ ) dependence for  $S_{cp}$  because  $S_{cp}$  is only weakly dependent on  $z$  as long as the field size ( $s$ ) is defined at depth in phantom (see. Eq. (9)).

Analogous to the factorization in Eq. (5), one can construct collision kerma factors as a mean to formalize primary and scatter separation, i.e.

$$D(z; s, d) = \frac{D(z; s, d)}{K(z; s, d)} \cdot \frac{K(z; s, d)}{K_p(z; s, d)} \cdot K_p(z; s, d) = \beta(z; s, d) \cdot SF(s, d) \cdot K_p(c; z; d), \quad (7)$$

where  $K$  and  $K_p$  are the collision kerma from all photons and the primary photons, respectively,  $\beta$  is the dose disequilibrium factor (or dose-to-collision kerma ratio), and  $SF = 1 + SPR$  is the scatter factor due to photon phantom scattering. The advantages of Eq. (7) are that  $SF$  is only a function of phantom (depth and irradiated field size) and is independent of source-to-detector distance,  $z$ ;  $K_p$  can be easily calculated since it is direct proportional to the incident energy fluence; and  $\beta$  is a constant at sufficient depths, under transient charged particle equilibrium. Applying Eq. (7) to Eq. (6) yield the expressions for  $TPR$  and  $S_{cp}$  as:

$$TPR(s, d) \equiv \frac{D(z; s, d)}{D(z; s, d_{ref})} = \beta(z; s, d) \cdot \frac{SF(s, d)}{SF(s, d_{ref})} \cdot \frac{K_p(d)}{K_p(d_{ref})} \quad (8)$$

and

$$S_{cp}(s) \equiv \frac{D(z; s, d_{ref})}{D(z; s_{ref}, d_{ref})} = \frac{SF(s, d_{ref})}{SF(s_{ref}, d_{ref})} \cdot \frac{K_p(c)}{K_p(c_{ref})} = S_p(s) \cdot S_c(c). \quad (9)$$

Using the separation of  $S_{cp}$  into  $S_p$  and  $S_c$  motivates the commonly used formalisms in the US<sup>12</sup>:

$$D(c; x, y, SDD; s, d) / M = TPR(s, d) \cdot S_p(s) \cdot S_c(c) \cdot POAR(x, y) \cdot INV(SDD) \cdot D(ref) / M, \quad (10)$$

where  $POAR$  is the primary off-axis ratio,  $s$  and  $c$  are the equivalent squares for the phantom scatter and the in-air output ratio for the point in an irregular field, respectively. Eq. (10), where the in-water output ratio  $S_{cp}$  is separated into a multiplication of  $S_p$  and  $S_c$ , clearly demonstrates the use of in-air output ratio in factor-based dose calculations.

## B. Dose-to-energy fluence formalisms

Realizing that the dose resulting from an irradiation is directly proportional to the amount of energy fluence incident onto the patient makes normalization of calculated dose per energy fluence appealing. Energy fluence is more practical than particle fluence since the kerma per energy fluence is relatively independent of photon energy, i.e. makes application of the formalism rather robust versus beam quality shifts. The appeal is accentuated realizing that both kernel based convolution/superposition models and Monte Carlo based calculations can be implemented using such formalism since the dose can be calculated per monitor unit following a “global” energy fluence to monitor units calibration. Details of such formalism has been outlined of Ahnesjö and co-workers<sup>13-16</sup> and Mackie *et al*<sup>17</sup>. The core of the dose calculation engine is supposed to deliver the quantity

$$d(x, y, z) = \frac{D(x, y, z | \Psi(A; x, y, z_{ref}))}{\Psi_0} \quad (11)$$

where  $D(x, y, z | \Psi(A; x, y, z_{ref}))$  is the absorbed dose at point  $(x, y, z)$ , given that the lateral energy fluence distribution for the field  $A$ ,  $\Psi(A; x, y, z_{ref})$ , is defined free in-air at a reference distance  $z_{ref}$  from the source, and  $\Psi_0$  is the energy fluence of direct particles free in-air at the isocenter. Following Ahnesjö<sup>15</sup>, the monitor units registered for a given beam can be separated into two parts,  $M_0$  and  $M_b$  where  $M_0$  is the signal proportional to the forward fluence through the monitor chamber and  $M_b = b(A) \cdot M_0$  is proportional to the fluence of particles back-scattered into the monitor from the upper part of the adjustable collimators. The total energy fluence delivered free in-air per monitor unit now follows as

$$\frac{\Psi(A; x, y, z_{ref})}{M} = \frac{\Psi(A; x, y, z_{ref})}{\Psi_0} \cdot \frac{\Psi_0}{M_0} \cdot (1 + b(A))^{-1} \quad (12)$$

The ratio  $\Psi_0/M_0$  is the key link between dose per energy fluence as calculated by a combined fluence/dose engine, to the dose per monitor unit as needed for monitor unit settings. The ratio is provided by a dose normalization for the reference geometry of the treatment unit, i.e.

$$\frac{\Psi_0}{M_0} = \frac{[D(A_{ref}; x_{ref}, y_{ref}, z_{ref}) / M]_{Measured}}{[D(A_{ref}; x_{ref}, y_{ref}, z_{ref}) / \Psi_0]_{Calculated}} \cdot (1 + b(A_{ref})) \quad (13)$$

Modelling of the energy fluence is commonly done separately for the direct and indirect photons, respectively. The direct photons are simply given by blocking collimated parts in a relative distribution of the direct photons for an uncollimated beam, to yield the relative distribution  $f(A; x, y, z_{ref})$ . Adding indirect photons,  $\Psi_{ind}$ , from irradiated parts of the treatment head then yields the total photon energy fluence of the beam:

$$\Psi(A; x, y, z_{ref}) = \Psi_0 \cdot \left( f(A; x, y, z_{ref}) + \frac{\Psi_{ind}}{\Psi_0}(A; x, y, z_{ref}) \right) \quad (14)$$

Equations (11) through (14) specify the models and data needed for implementation of the formalism. Incident energy fluence must drive dose calculations to yield dose, the relative energy fluence distribution  $f$  of direct particles must be known, the indirect component  $\Psi_{ind}/\Psi_0$  as well as the collimator backscatter to the monitor through  $b(c)$  should be provided.

The role for measured data is to determine the necessary data of fluence variations with field settings,

$$S_c \approx \frac{\Psi_0 + \Psi_{ind}(A)}{\Psi_0 + \Psi_{ind}(A_{ref})} \cdot \frac{(1+b(A_{ref}))}{(1+b(A))}, \quad (15)$$

which commonly is used to match model results while determining parameters for head scatter models. In the following section, we will review the main physical determining the output.

## IV. PHOTON BEAM CHARACTERISTICS

First principle models give the absolute dose per impinging energy fluence and dose determination would be trivial if the fluence could be monitored directly. In practice fluence monitoring is non-trivial since scattered photons from the treatment head add an "unmonitored" contribution  $\Psi_{ind}$  to the fluence, and backscatter into the monitor yields a "false" contribution  $M_b$  to the total signal, i.e.

$$\frac{\Psi}{M} = \frac{\Psi_0 + \Psi_{ind}}{M_0 + M_b}. \quad (16)$$

Hence, the monitoring which provides  $M_0$  must be complemented with models for  $\Psi_{ind}$  and  $M_b$  to yield dose per monitor unit calculations.

### A. Direct beam characteristics

A slightly more explicit form of the fluence part of Eq. (16) is

$$\Psi(A; x, y) = \Psi_0 \left( \eta(A; x, y) \cdot f(x, y) + \frac{\Psi_f(A; x, y) + \Psi_c(A; x, y) + \Psi_m(A; x, y)}{\Psi_0} \right) \quad (17)$$

where  $\eta(A; x, y)$  is the modulation at the lateral position  $(x, y)$  caused by field  $A$  onto the relative distribution of the un-collimated, direct beam  $f(x, y)$ . The headscatter parts  $\Psi_f$ ,  $\Psi_c$  and  $\Psi_m$  represents the contributions from the most important sources the flattening filter, the collimators and the modulators (e.g. wedge), respectively. In convolution/superposition dose modeling, the calculation is done one in three distinctive steps. First is the output fluence modeled, followed by a calculation of the energy released from the beam. In the last step, the released energy is further transported and deposited as dose by means of energy deposition kernels. The energy fluence is typically raytraced, and the energy released from the direct particles (i.e. those without patient interaction history but including headscatter, see Fig. 1) is calculated using exponential attenuation. As an example, the collision kerma can be calculated as

$$P(z) = \sum_{i=1}^n \Psi_{E_i} \frac{\mu_{en}(E_i)}{\rho} e^{-\mu(E_i)z} \Delta E = \Psi \frac{\bar{\mu}_{en}}{\rho} \cdot e^{-\mu_p(1-\kappa_p)z} \quad (18)$$

where  $\Psi_{E_i} \Delta E$  is the energy fluence of spectral bin  $i$  with energy absorption  $\mu_{en}(E_i)$  and attenuation  $\mu(E_i)$  coefficients, respectively. Summing over the spectrum enables use of a single exponential with effective attenuation  $\mu_p$ , depth hardening  $\kappa_p$  and average energy absorption coefficient  $\bar{\mu}_{en}$ . The lateral variation of the energy fluence can be estimated by the same experimental technique as for  $S_c$  measurements which yield a kerma biased fluence ratio. This simplifies calculations since lateral variations in  $\bar{\mu}_{en}$  not need to be explicitly modeled:

$$\frac{\Psi \frac{\bar{\mu}_{en}}{\rho}}{\left( \Psi \frac{\bar{\mu}_{en}}{\rho} \right)_{ref}} = \Psi \frac{\bar{\mu}_{en}}{(\bar{\mu}_{en})_{ref}} \cdot \frac{(\bar{\mu}_{en})_{ref}}{\rho} \quad (19)$$

Hence,  $f(x, y)$  in Eq. (17) can be interpreted as the relative distribution of the collision kerma biased energy fluence distribution. The determination of  $\eta(A; x, y)$  in Eq. (17) is straight forward for the collimation part – blocked parts of the beam are assigned a fluence value proportional to collimator leakage and open parts  $\eta(A; x, y)$  are assigned to unity. Using modulators, the actual values can be measured or calculated with a variety of methods, beyond the scope of this presentation.

## **B. Photon headscattering ( $\psi_{\text{ind}}$ )**

### **1. Photon scatter from the flattening filter and primary collimator**

Measurements,<sup>3, 5, 7-9, 18-22</sup> Monte Carlo simulations,<sup>23, 24</sup> and analytic approximations<sup>13</sup> have all established the role of the flattening filter and the primary collimator/beam dump to act as a distributed source which may contribute up to 12% of the output photons. The variation of the in-air output ratio with field setting and position can be explained by means of an extended source integration over the parts visible from the calculation's point view<sup>7, 9, 13, 15, 22, 24, 27</sup>, see Fig 1a,b and c.

Different shapes of the extended source intensity distribution have been used, such as triangular, constant or Gaussian yielding similar results indicating that the overall amount of filter scatter is more important than the particular shape used to model it. These characteristics of photon beams are due to a partial eclipsing of the extrafocal source component by the field defining collimators. Since the flattening filter is both located downstream of the target, and extended, its radiation will reach outside of the beam collimation where it will dominate since the collimator leakage contribution is less. It must be emphasized that because the dose contribution from headscatter photons partly dominates the fluence distribution outside of beam collimation, accounting for indirect radiation is very important for the prediction of dose in such locations. This is especially important for IMRT since the dose contribution in low dose region is dominantly determined by the headscatter. A headscatter model to predict  $S_c$  correctly at off-axis points is thus very important to accurately predict the dose at off-axis points. This is illustrated in Fig 1c. Recent experimental data confirms these findings and several studies have shown that up to 2% variation in  $S_c$  values can be seen at off-axis locations.<sup>21, 28-30</sup> Measurements suggest that the variation of headscatter photons at the off-axis points is more complicated than a simple Gaussian distribution,<sup>28</sup> and requires two Gaussian sources instead of one to describe the distribution correctly.<sup>28</sup> Monte-Carlo simulation can successfully predict the distribution of headscatter within beam collimation, but has underestimated the results outside beam collimation (see Fig. 2).

Variation in flattening filter view (together with backscatter variations to the monitor) constitutes the main explanation for the collimator exchange effect. Experimentally, it refers to the phenomenon that when defining a rectangular radiation field, the in-air output ratio differs depending on which side of the rectangular delineate the inner and outer collimator jaws (i.e.  $c_x \times c_y$  or  $c_y \times c_x$ ).<sup>33</sup> It has been shown the collimator exchange coefficient varies between 1.2 and 1.8 for the major accelerator types.<sup>36</sup> Thatcher and Bjärngård<sup>52</sup> pointed out that blocks, in general, should have negligible effects on  $S_c$  (at most 1% change for most clinic cases including extreme blocks) because the collimator jaws are located closer to the location of the flattening filter than the blocks, thus it is the collimator jaws rather than the blocks that influence the amount of headscatter from the flattening filter.

Since the flattening filter scatter may constitute up to 12% of the output photon radiation, its location downstream of target it will influence the variation of incident radiation as a function of distance to the x-ray source, a phenomena that can be modeled through a virtual change in source position. It has in one case been shown that the shift was about 1 cm for open field and about 2 to 3 cm for wedged field.<sup>6</sup> A more detailed study to examine the correlation between  $S_c$  and SDD showed that the change in  $S_c$  for open beam at different SDD is in deed very small (< 1%) for SDD up to 300 cm.<sup>38</sup> A similar study for wedge beams estimated an effect in  $S_c$  of about 2% for wedged beams.<sup>39</sup>

## 2. Wedge and Compensator scatter

Second to structures closest to the target, hard wedges or compensating filters are the most important scatter sources in clinical beams. The presence of a wedge increases the fraction of "headscattered" photons and, thus, the value of  $S_c$  in a high-energy x-ray beam.<sup>7</sup> Huang *et al.*<sup>41</sup> determined experimentally the component of the dose caused by photons scattered in the wedge. Thomas<sup>42</sup> commented on this work by stressing the importance of whether the wedge is mounted internally, i.e. between the source and the collimators, or externally. One can anticipate differences between these two cases. An internal wedge is inside the collimator head and always completely irradiated but not always completely seen through the collimator opening, while an external wedge, which is close to the patient, is irradiated only by the collimated beam but always completely seen from the point of interest. Zhu *et al.*<sup>40</sup> have provided some empirical expressions to model the headscatter from internal and external wedges appropriately (see Fig. 3):

$$SPR(c) = \begin{cases} a_2 \cdot erf(c/\lambda)^2 & \text{(internal wedge)} \\ \alpha \cdot (c/40)^2 & \text{(external wedge)} \end{cases}, \quad (20)$$

where  $a_2$ ,  $\alpha$  and  $\lambda$  are constant parameters.  $SPR$  is the ratio of headscatter-to-direct radiation for the wedge. The parameters  $a_2$  (or  $\alpha$ ) determines the maximum  $SPR$  for the largest field ( $40 \times 40$  cm<sup>2</sup>). Analytical calculation models based on first scatter integration over the scattering device<sup>14, 43</sup>, and an "extended phantom concept" using precalculated modulator kernels superimposed over the modulator within the calculation point of view<sup>44</sup> have all shown good results. Monte Carlo simulations confirm and bring further details to these results. Schach von Wittenau *et al.*<sup>45</sup> investigated to which degree Monte Carlo simulations can be approximated without changing the result.

Van der Zee and Welleweerd<sup>46</sup> simulated the Elekta internal wedge. They found that the presence of the wedge altered the direct and scattered photon components from the linac significantly: beam hardening shifted the mean photon energy by 0.3 MeV and 0.7 MeV was observed for the two components, respectively. They also analysed the wedge influence and consequences for use of output ratios in factor based dose calculations and formulated recommendations regarding their use. Verhaegen and Das<sup>47</sup>, Shih *et al.*<sup>48, 49</sup> and Ma *et al.*<sup>50</sup> have investigated Dynamic and Virtual wedges and proved that no significant spectral changes were imposed, as a contrast to physical wedges.

## 3. Collimator scatter and leakage

In most cases scatter contributions from the movable collimators are of the order of less than 1% to the total dose and hence is relatively insignificant. But the collimators play a very important role in defining scatter contributions from the treatment head including the target, the primary collimator and the flattening filter. Photon backscatter from the jaws into the monitor chamber may have an effect on accelerator output for some accelerators but it is negligible from the MLC. Photon leakage through the jaws is generally less than 0.5% while it can be 1-2% through the MLC leaves with a dominating part from interleaf leakage. Furthermore, the MLC tongue and groove geometry and the shape of the leaf ends may cause additional leakage and scatter.

Detailed jaw and MLC geometries have been studied using Monte Carlo simulation for different accelerators<sup>124-127</sup>. Good agreement was achieved between Monte Carlo calculations and film and ion chamber measurements. No significant spectral differences were noted when large and small fields were compared. Deng *et al.*<sup>128</sup> studied the MLC tongue-and-groove effect on IMRT dose distributions. They used a ray-tracing approach to derive the fluence maps for an IMRT plan based on the actual leaf sequence and MLC leaf geometry. Their results suggest that the effect of the tongue-and-groove geometry is probably insignificant in IMRT with multiple gantry angles, especially when organ/patient movement is considered.

Several experimental studies performed for the conventional blocks and secondary collimator jaws confirmed the above conclusions.<sup>7, 51-54</sup> Zhu and Bjärngard<sup>7</sup> have demonstrated experimentally that the headscatter from the collimator jaws alone provides less than 1% of total output variation by physically removing the flattening filter.

### C. Monitor backscattering

The monitor backscatter has been studied by a variety of experimental methods. Techniques for measuring  $S_b$  include activation of metal foils<sup>19</sup>, using a pin-hole telescope aimed at the target<sup>55-58</sup>, comparing the difference between output with and without an acrylic filter between the chamber and the jaws<sup>20</sup>, counting beam pulses<sup>9, 58, 59</sup>, measuring beam current<sup>60</sup> and measuring beam charge<sup>57</sup>. Kubo<sup>55</sup> used a telescopic technique to exclude the scattered components from the readout of an external detector and measured the variation in monitor units delivered per unit external signal. For a Clinac 1800 he found small variations in the order of 1% to 2% but for a Therac 20 machine the backscatter variation was as high as 7.5% between a 2×2 cm<sup>2</sup> field and a 40×40 cm<sup>2</sup> field (see Fig. 4). Hounsell<sup>61</sup> also used a telescopic technique and found small variations of the order of less than 1% for an Elekta-Philips SL15 with a protection sheet (3 mm Al) in place between the collimators and the monitor chamber, but a considerably higher variation when the protection sheet was removed, approximately 5% between a 4×4 cm<sup>2</sup> and 40×40 cm<sup>2</sup> field. Several investigators<sup>9, 58, 62</sup> used the number of linac pulses as independent measure of the primary fluence and found that the monitor backscatter signal varied between 2% and 5% for the largest and smallest fields with a kapton window monitor chamber. When a protection sheet of aluminium was set in place to stop low energy charged particles the variation reduced to 0.5%-1.0%. Yu *et al* applied this technique to a Varian Clinac 600C and a 2100C and found a variation of approximately 2 % for the upper jaws and 1 % for the lower pair of jaws at energies above 15 MV and about half those values for 6 MV. Lam<sup>57</sup> measured the target charge needed to deliver a given amount of monitor units as a function of collimator setting, as it was considered more reliable than the number of linac pulses. On a Varian Clinac 2100C they found a 2.4% variation for the upper jaws and 1.0% variation for the lower pair of jaws.

The backscatter signal fraction  $b=M_b/M_0$  (cf Eq. (16)) has been modeled by Ahnesjö *et al*<sup>15</sup> assuming that it can be determined by a proportionality factor  $k_b$  times a geometry factor for diffuse radiation, such that

$$b = k_b \frac{z_{SMD}^2}{z_{SCD}^2} \iint \frac{\cos^3 \theta_A}{\pi \cdot z_{MCD}^2} dA_{irr} \quad (21)$$

where  $z_{SMD}$  is the source to monitor distance,  $z_{SCD}$  is the distance from the source to the backscattering collimator surface,  $z_{MCD}$  is the monitor to backscattering surface distance,  $\theta_A$  is the angle between the normal of the backscattering element  $dA$  and its view vector of the monitor and  $A_{irr}$  is the irradiated backscattering area (in the original paper the source to isocenter distance was erroneously used instead of  $z_{SMD}$  and the reflected radiation stated to be isotropic rather than diffuse). A comparison of data from the work by Lam *et al*<sup>57</sup> with Eq. (20) yields  $k_b$  values on the order of 0.3 to 0.4 for kapton windowed chambers and approximately zero for chambers with metal sheet windows. Neglecting the cosine factor in the integrand of Eq. (20) reduces it to an area calculation particularly simple to implement.

### D. Source obscuring effect

For very small collimator settings (usually less than 2 × 2 cm<sup>2</sup>), the actual x-ray source is partially obscured by the collimator jaws resulting in a substantial reduction of the output.<sup>63</sup>  $S_c$  reduces to zero when the collimator jaws are completely closed. The source-obscuring effect dominates the output ratio of stereotactic radiosurgery using linear accelerator<sup>64</sup> and gamma knife<sup>65</sup>. For these situations, it is important to consider additional output reduction through loss of lateral electron equilibrium and partial irradiation of the detector.

The source size is an important input parameter for Monte-Carlo or analytical theory to model the effect of the x-ray source size on output (for small fields) or the penumbra shape. They are best extrapolated from measurements.

Figure 5 shows the measured  $S_c$  for several different accelerators.<sup>63</sup> The greatest effect is shown for the Clinac-6/100 which has no bending magnet and the next the SL75-5 with a 90° permanent bending magnet. The SL25 has a 90° bending magnet as well, but it is preceded by a "slalom" magnet arrangement. The Clinac-1800 with a 270° bending magnet and an electron slit shows the smallest effect and has the smallest x-ray source size among the accelerators examined. All these measurements were made at extended SSD using a lead miniphantom with lateral diameter of less than 1 cm.

## V. MEASUREMENT OF IN-AIR OUTPUT RATIO

### A. Measurement of the effect of miniphantom on $S_c$

Detectors need walls thick enough to provide electronic equilibrium in order to convert ionization reading to dose. As noted previously, the original in-air measurements to determine  $S_c$  used build-up caps to bring the thickness to detector walls to equilibrium. Materials used include acrylic, polystyrene, water-equivalent plastics, graphite, lead, tungsten, copper (brass), and aluminum. Coverings made of water-equivalent material, although more relevant to clinical interest, are generally not suitable for small field sizes. To reduce the physical size, the coverings are sometime made of high-Z materials. However, it has been argued that the high-Z materials may alter beam spectra change and thus introduce errors in the measurement.<sup>11, 66</sup> Several investigators have studied the influence of build-up cap material on the measurement of  $S_c$ .<sup>67, 68</sup> Frye *et al*<sup>67</sup> reported significant differences (up to 4.8% for a 24 MV beam) between the measurements of using build-up caps made of Solid Water and those with graphite buildup caps. Using magnetic field to sweep the contaminate electrons in the 24 MV beam, they concluded that a significant portion of the difference was, indeed, contributed from the contaminated electrons. By comparing measurements with build-up caps made of low- and high-Z materials (lead and brass), Weber *et al*<sup>69</sup> observed deviations of up to  $\pm 1\%$  in the  $S_c$  values for high-energy beams (see Fig. 6). They reported that the thicknesses of their build-up caps were sufficient to stop contaminating electrons. Based on a similar measurement, Jursinic and Thomasen<sup>68</sup> found larger differences (up to 4%) between their lead-cap and acrylic-cap measurements for a 18 MV beam with large field sizes. These increased differences are most likely due to the contributions from contaminating electrons, as the wall thicknesses of their caps were equal to maximum dose build-up depths. Thomadsen *et al*<sup>70</sup> reported that electron contamination penetrates considerable farther than the depth of equilibrium, and for a 24 MV beam, some contamination reaches 10 cm. The thrust of all this work implies that conventional build-up cap fail to provide the basic requirement for  $S_c$  determination: a signal proportional to the incident photon energy fluence. Venselarr *et al*<sup>71</sup> have shown the field size dependence of  $S_c$  is affected by electron contamination, if insufficient thickness is used in the miniphantom.

It can be concluded, based on these studies, that the most important factor in the measurement of  $S_c$  is the use of a cap with a thickness sufficient to prevent contaminating electrons from reaching the detector. Van Gasteren *et al*<sup>11</sup> has shown that once the buildup is thick enough, which they referred to as miniphantoms,  $S_c$  can be reliably measured for water-equivalent materials (acrylic, polystyrene, and water-equivalent plastics). The choice of phantom materials also has some influence on the results. Miniphantoms made of low-Z materials are generally recommended, as discussed above, because the conversion from photon energy fluence to kerma in water depends on the water-equivalent attenuation coefficient. One requirement of this approach to  $S_c$  measurement is that the radiation field edges much exceed the miniphantom lateral dimension. As long as this is the case, the fractional signal generated by the phantom scatter generated by the miniphantom will be the same in the numerator and the denominator of the equation used to calculate  $S_c$  and cancel out. To extend the range of  $S_c$  to smaller field sizes, one approach has been to use higher density, higher atomic-number miniphantoms. Li *et al*<sup>72</sup> have compared the measurements with using cylindrical miniphantoms made of polystyrene or brass. Their data shows that, as long as the miniphantoms are

constructed to prevent contaminated electrons reaching the detector, the measurements with polystyrene and brass miniphantoms agree within 0.5% for both a 6 and an 18 MV beams. The magnitude of differences produced by miniphantoms made of high Z material increases with collimator setting, being small for collimator settings less than  $6 \times 6 \text{ cm}^2$ , but rising to the 1% level for a  $40 \times 40 \text{ cm}^2$  field. This conclusion is also supported by other measurements. In a comparison of  $S_c$  measurements between lead and acrylic miniphantom, no differences were found between the two for small collimator settings.<sup>63</sup>

Usually, the  $S_c$  value is measured by an ionization chamber situated within a miniphantom. Two types of miniphantoms are commonly used: (1) conventional buildup caps of varying composition and thickness, and (2) coaxial columnar miniphantoms of different material and size. It has been reported that the physical shape, dimension and composition of a miniphantom can influence the  $S_c$  value determined with the miniphantom<sup>11, 67-69</sup>. This effect can be characterized by the Monte Carlo methods. Particularly, the Monte Carlo methods can be used to identify the sources of the influence and to calculate corrections if necessary. Johnsson and Ceberg has performed a Monte-Carlo study on the effect of water-equivalent miniphantom thickness on the accuracy of transmission measurement.<sup>73</sup> They defined a measured quantity as the collision kerma in-water in a point in free space, similar to the definition of the incident output function. They reported a range of miniphantom depths for specific photon energy in order to obtain accurate measurement of transmission to within 1%. However, the limit of phantom thickness on  $S_c$  is likely to be much relaxed because the photon energy spectra do not change as much as that for the transmission measurements. Experimental studies have shown no effect of phantom thickness on  $S_c$ , provided sufficient thickness for CPE.<sup>11</sup> At the time of this report writing, the task group was not aware of any publication in the literature that addresses the Monte Carlo simulation of miniphantoms specifically for  $S_c$ .

A method to produce a correct curve for  $S_c$  may be the following: Use a water-equivalent detector from the largest field sizes to the field size that just exscribes the diameter of the miniphantom. From below that size, use a high-density (and thus a high atomic-number) miniphantom with a small detector, allowing extension to field sizes again just exscribes the diameter of the high-density miniphantom. Dividing the reading for the small field size by that for a  $4 \times 4 \text{ cm}$  field and then multiplying by the  $S_c$  for the  $4 \times 4 \text{ cm}^2$  field allows extrapolation to these smaller field sizes because the relative readings differ little below the  $4 \times 4 \text{ cm}^2$ . The high-density miniphantoms must present the same projected, radiological profile as the water-equivalent miniphantom. That would mean that all of the linear dimensions should be scaled by the ratio of the linear attenuation coefficient for the high-density material to that of water.

### ***B Influence of detectors on measurement of $S_c$***

Various detectors (e.g., ionization chamber and diode) have been used to measure  $S_c$ .  $S_c$  curves measured with diode detectors, shielded or unshielded, give identical results as that of an ionization chamber.<sup>74</sup> It is also reported that the orientation of ionization chamber (whether its axis is perpendicular or parallel to incident radiation) does not affect the measured results.<sup>28, 68</sup>

### ***C Recommendation of miniphantom dimension for $S_c$***

For most field sizes,  $S_c$  measurements should be made with the detector in a miniphantom as shown in Fig. 8, mostly made of a water-equivalent material such as solid water, acrylic, graphite, or PMMA, with  $4 \text{ g/cm}^2$  diameter cross section with the detector at  $10 \text{ g/cm}^2$  depth, as described by van Gasteren *et al*<sup>11</sup> and the ESTRO protocol<sup>1</sup>. The detector and miniphantom should be supported on a low density stand (e.g. Styrofoam) to minimize room scatter into the detector volume.

For small collimator settings ( $c < 4 \text{ cm}$ ), miniphantom made of high Z material (such as lead or brass) can be used. The lateral dimension has to be sufficient thick ( $>4 \text{ g/cm}^2$ ) to maintain lateral CPE. The longitudinal

dimension should be sufficient thick (10 g/cm<sup>2</sup>) to maintain longitudinal CPE and eliminate contaminant electrons.

To provide lateral CPE for the small segment fields that are common in IMRT, a high-density miniphantom may be used. Brass (approximately 63% Cu, 37% Zn) is an appealing alloy comprising high density (8.4 g·cm<sup>-3</sup>) with moderate atomic numbers (29 and 30), good machinability and well known dosimetric properties<sup>69, 72, 75</sup>. However, the introduction of high Z material changes the response since the detector is exposed to charged particle fluence released from the high Z material, not from water. Hence, the in-air output ratio is experimentally determined as the dose corrected ratio<sup>75</sup> from high density capped detectors, such that influence from electron contamination is excluded. When the beam quality is constant (i.e. ratios for open-to-open fields, or wedge-to-wedge fields), the ionization to dose correction values canceled out, making the procedure particularly simple to employ clinically. It is estimated that the use of brass miniphantom instead of water equivalent material introduces about 1% of change for  $S_c$ .<sup>69</sup>

When high Z materials are used as a miniphantom, the measured value may deviate from the true value for  $S_c$ . However, it is often desirable to use miniphantoms with small dimensions for measurements in small fields while still maintaining sufficient thickness for electron equilibrium and to eliminate contaminant electrons. With proper care, one may be able to define a range of collimator settings where high Z miniphantoms can be used for  $S_c$ . Figure 9 shows the schematics of a brass miniphantom suitable for measurement of small field sizes.

## VI EMPIRICAL METHODS FOR CHARACTERIZATION OF $S_c$

### *A. Empirical modelling of multiple photon sources and monitor backscattering*

$S_c$  expresses how the incident or primary photon fluence per monitor unit (or unit time for a Co-60 unit) varies with collimator setting. The physical reasons for this variation have been studied using empirical modeling<sup>3, 7, 9, 22, 37, 76</sup>, semi-analytical modeling<sup>13, 77</sup>, and Monte-Carlo simulation<sup>24, 27, 62</sup>.

The behavior of headscatter as a function of collimator opening is consistent with models that assume that the source is Gaussian and lies downstream from the target<sup>22</sup>, and it has been demonstrated that the beam-flattening filter is the major source of headscatter photons. If a physical wedge or other material is inserted in the beam, the headscatter increases,<sup>7</sup> and the virtual source may be additionally displaced from the nominal source.<sup>6, 38</sup>

The source-obscuration effect is only relevant for very small collimator settings (usually less than  $2 \times 2$  cm<sup>2</sup>), but then it becomes the dominating effect and reduces the output ratio in-air to zero when the collimators are closed. It has been described by Zhu *et al.*<sup>63, 78</sup>

The monitor-backscatter effect can be measured by operating the accelerator without the dose-rate servo-control<sup>59</sup>, by using a “telescope” method<sup>55, 56, 58</sup>, by target-current pulse counting<sup>58</sup>, by using the target charge method<sup>57</sup>, or by photoactivation of copper placed above the flattening filter<sup>19</sup>. The first two methods do not require opening up the accelerator head or special electronic instruments and can achieve a reproducibility of 0.3%, but they are still very time-consuming. — The monitor backscatter differs for different accelerator models. For some Varian accelerators, the maximum contribution from the monitor backscatter can be large (3 - 5 %).<sup>56</sup>

Several headscatter models have been successfully used to predict  $S_c$  on the central-axis. These models use a set of measurements from square collimator settings to extract the necessary parameter. One example of such model uses three parameters to calculate  $S_c$ , the output ratio on the central-axis is<sup>36</sup>

$$S_c = \frac{(1 + a_1 \cdot c) \cdot (1 + SPR_{air}(cx, cy))}{(1 + a_1 \cdot 10) \cdot (1 + SPR_{air}(10, 10))} = (1 + a_1 \cdot c) \cdot (1 + SPR_{air}(cx, cy)) \cdot H_0, \quad (22)$$

where  $H_0$  is a normalization constant that sets  $S_c = 1$  at the collimator setting  $10 \times 10$  cm<sup>2</sup>, i.e.,  $1/(1 + a_1 \cdot 10) \cdot (1 + a_2 \cdot erf(10/\lambda)^2)$ .  $a_2$  is the maximum scatter-to-primary ratio, i.e. if  $a_2 = 0.10$ , 10% of the incident fluence is indirect radiation.  $a_1$  is the monitor-backscatter coefficient. Typical parameters for a range of linear accelerators can be found in Table 2. The direct kerma measured in the miniphantom is separated into the direct  $K_d$  and the indirect (or headscatter)  $K_h$  components such that  $K_{air} = K_d + K_h = K_d \cdot (1 + SPR_{air})$ . Notice  $c$  in Eq. (22) is the equivalent square calculated from the collimator jaws using Eq. 22:

$$c = (1 + k) \cdot c_y \cdot c_x / (k \cdot c_x + c_y). \quad (23)$$

Here  $c_x$  and  $c_y$  denote the settings of the outer and inner collimators, respectively, and  $k$  ( $>1$ ) is the collimator-exchange coefficient. If only the headscatter photons are considered, the collimator-exchange coefficient can be determined from the head geometry as<sup>35</sup>:

$$k = l_x \cdot (SDD - l_y) / l_y \cdot (SDD - l_x), \quad (24)$$

where  $l_x$  and  $l_y$  are the source-to-collimator distances for outer and inner collimators, and  $SDD$  is the source-to-detector distance. The value of  $k$  can be determined experimentally for the Elekta<sup>34</sup> and Varian<sup>35</sup> accelerators to be 1.8. However, the collimator-exchange coefficient for a particular type of accelerator may be different from this value. It has been shown the collimator exchange coefficient varies between 1.2 and 1.8 for the major accelerator types.<sup>36</sup> Other formalisms have also been proposed to calculate  $S_c$  for rectangular fields.<sup>37</sup>

### ***B. $S_c$ for MLC shaped fields***

The Multileaf Collimator (MLC) has movable abutting leaves to generate any arbitrarily shaped field. Typical MLCs have 20 to 120 leaves arranged as pairs in two banks. The most common application of MLC is to replace conventional blocking. The field-shaping function with MLC is accomplished using leaf position sets stored on a computer file. These files can be created especially for a given field to be applied to a specific patient in analogy to the fabrication of cerrobend blocks. The other application of the MLC is to achieve beam-intensity modulation. This is accomplished by using either the motion of the MLC leaves during irradiation or by using multiple small static MLC field segment irradiations at a fixed gantry position.

The use of an MLC for field shaping does not change the way the in-phantom scatter is computed. The in-phantom scatter depends on the final field size projected on the patient and the methods for calculating scatter dose in the patient are well established. However, the in-air output for MLC shaped fields is dependent upon the design and the geometry of the MLC system. It is well understood that the major contributor of scatter radiation to the in-air output of a medical linear accelerator are the primary collimator, flattening filter, and tertiary collimator. The amount of scatter radiation reaching a point downstream from a MLC system depends on the area of the extra-focal radiation source as seen by this point through different levels of collimators. For linear accelerators equipped with conventional jaws, because the upper collimator jaws are closer to the source than the lower jaws, the same size of opening made by the upper and the lower jaws in the beams-eye-view (BEV) are different when viewed from the point of calculation. A collimator setting that projects a square field into the BEV will project a rectangle when viewed from the point of calculation to a plane at the bottom of the flattening filter. Similarly, the position of the MLC in the treatment head determines how the in-air output ratios can be calculated accurately. When an MLC is implemented as an upper or lower jaw replacement of a secondary collimator, the MLC affects the output ratio much more strongly. The radiation field is defined jointly by both the MLC and the remaining set of jaws. The in-air

output ratios must then be calculated using the irregular field shape instead of the rectangular field circumscribing it. Depending on which set of jaws the MLC is replacing different methods should be used. If the MLC is located at the position of the upper jaws in the secondary collimator, as in the Elekta MLC design, the irregular field shape determines both the head scatter and the phantom scatter. In the Elekta design, there is a pair of backup jaws situated under the MLC leaves and motorized to travel in the same direction as the leaves. These backup jaws serve to minimize the interleaf transmission outside the radiation field. These jaws are normally set at the same position as the outermost leaves and make only a small contribution to the head scatter. The lower jaws, which move in a direction perpendicular to that of the leaf travel, define the beam aperture in that dimension and block the transmission from the gap between the ends of any opposing banks of leaves outside the radiation field. The lower jaws generally do not restrict the view of the extended extra-focal source from the calculation point. This is because the leaves above the lower jaws are set at closed positions outside the radiation field. Therefore, the in-air output ratio is determined mainly by the MLC shapes. Palta *et al*<sup>79</sup> showed that the in-air output ratio for shaped fields with Elekta MLC can be accurately calculated using an equivalent square<sup>80</sup> of the MLC-shaped field. The equivalent square for the MLC-shaped field can be readily calculated using Clarkson sector integration method<sup>81</sup> if it is assumed that the source of extra-focal radiation is radially symmetric. It is important to note that the integration method is valid only when the field dimensions in both the measurements and the calculations are projected from the calculation point back through the collimation system to the effective source plane of extra-focal radiation<sup>35</sup>.

If the MLC replaces the lower jaws in the secondary collimator, as in the MLC design of Siemens, both the MLC leaf positions and the upper jaw positions determine the in-air output ratio. Since the jaws are closer to the effective collimator scatter source, they define the field aperture in the dimension perpendicular to the direction of leaf travel in both the BEV and in the projection of the calculation points. Unlike the MLC design where the MLC replaces the upper jaws, different field shapes should be used for determining the in-air and in-phantom scatter parameters. The in-air output ratio should be determined from the irregular fields viewed from the calculation point.

When the MLC is used as a tertiary collimator along with the upper and the lower collimator, as in the design of Varian, the field shape defined by the MLC is closer to the plane of any given calculation point than the upper or lower jaws. Unless the MLC-shaped field is substantially smaller than the rectangular field formed by the upper and lower collimator jaws, the tertiary blocking boundary will not affect the projection of the field size from the calculation point back to the effective source of extra-focal radiation. In this case, the jaw openings determine the in-air output ratio.<sup>82</sup> However, Kim *et al*<sup>3</sup> have shown that the scatter radiation contribution from the tertiary MLC to the in-air output ratio for small MLC-shaped fields may not be negligible. This is often the case in small beam apertures used for intensity modulation.

## VII QUALITY ASSURANCE

Quality assurance has a crucial role in all aspects of radiation oncology, as outlined in the report of AAPM Task Group 40. In this section, quality assurance techniques used in the measurement of output ratio are described. This section will discuss various methods existed in the literature to quality assurance  $S_c$ . This includes, primarily two categories of methods: (a) accumulative database of  $S_c$  measured from different accelerators (b) characterize the range of parameters suitable for a particular accelerator.

Large data base of measured in-air output ratio existed in the literature for the open and wedged beams of the major accelerator vendors and the Cobalt machines.<sup>36</sup> These data can be used as a verification tool to ensure that the magnitude of the measured in-air output ratio is not entirely out of order.

It is more convenient to QA gross error in measured output ratio by parameterize the in-air output ratio using a model, such as Eq. 23. One can establish the range of the three parameters ( $a_1$ ,  $a_2$ , and  $\lambda$ ) for a given accelerator (Table 2). These parameters can be compared with the parameterization established from the measured value to see if it is reasonable or not.

With proper quality assurance, one should be able to determine  $S_c$  for square fields to within an accuracy of 1%.  $S_c$  should be checked annually or whenever major change has been made to a linear accelerator to ensure that it has not changed.

## VIII. Acknowledgment

The author wishes to thank members of the AAPM RTC task group 74 for their contributions to establish a methodology to measure and interpret the in-air output ratio.

## IX Bibliography

- <sup>1</sup>A. Dutreix, B. E. Bjärngard, A. Bridier, B. Mijnheer, J. E. Shaw, and H. Svensson, *Monitor Unit Calculation For High Energy Photon Beams*, (Garant Publishers, N. V., Leuven/Apeldoorn, 1997).
- <sup>2</sup>J. G. Holt, J. S. Laughlin, and J. P. Moroney, "The extension of the concept of tissue-air ratios (TAR) to high-energy x-ray beams," *Radiology* **96**, 437-446 (1970).
- <sup>3</sup>S. Kim, J. R. Palta, and T. C. Zhu, "A generalized solution for the calculation of in-air output factors in irregular fields," *Medical Physics* **25**, 1692-1701 (1998).
- <sup>4</sup>F. Khan, *The Physics of Radiation Therapy*, 2nd Ed. Ed. (Williams & Wilkins, Baltimore, MD, 1994).
- <sup>5</sup>K. R. Kase, and G. K. Svensson, "Head scatter data for several linear accelerators (4 - 18 MV)," *Med Phys* **13**, 530-532 (1986).
- <sup>6</sup>M. Tatcher, and B. E. Bjärngard, "Head-scatter factors and effective x-ray source positions in a 25-MV linear accelerator," *Med Phys* **19**, 685-686 (1992).
- <sup>7</sup>T. C. Zhu, and B. E. Bjärngard, "The fraction of photons undergoing head scatter in x-ray beams," *Phys Med Biol* **40**, 1127-1134 (1995).
- <sup>8</sup>D. A. Jaffray, Battista, J. J., Fenster, A., Munro, P., "X-ray sources of medical linear accelerators: Focal and extra-focal radiation," *Medical Physics* **20**, 1417-1427 (1993).
- <sup>9</sup>M. B. Sharpe, D. A. Jaffray, J. J. Battista, and P. Munro, "Extrafocal radiation: A unified approach to the prediction of beam penumbra and output factors for megavoltage x-ray beams," *Med Phys* **22**, 2065-2074 (1995).
- <sup>10</sup>T. C. Zhu, Manbeck, K., "CT reconstruction of x-ray source profile of a medical accelerator," *Proc. SPIE* **2132**, 242-253 (1994).
- <sup>11</sup>J. J. M. van Gasteren, S. Heukelom, H. J. van Kleffens, R. van der Laarse, J. L. M. Venselaar, and C. F. Westerman, "The determination of phantom and collimator scatter components of the output of megavoltage photon beams: measurement of the collimator scatter part with a beam-coaxial narrow cylindrical phantom," *Radiother Oncol* **20**, 250-257 (1991).
- <sup>12</sup>J. Gibbons (TG74), *MU calculation for photon and electron beams*, (AAPM, College Park, MD, 2004).
- <sup>13</sup>A. Ahnesjö, "Analytic modelling of photon scatter from flattening filters in photon therapy beams," *Med Phys* **21**, 1227-1235 (1994).
- <sup>14</sup>A. Ahnesjö, L. Weber, and P. Nilsson, "Modelling transmission and scatter for photon beam attenuators," *Med Phys* **22**, 1711-1720 (1995).
- <sup>15</sup>A. Ahnesjö, T. Knöös, and A. Montelius, "Application of the convolution method for calculation of output factors for therapy photon beams," *Med Phys* **19**, 295-304 (1992).
- <sup>16</sup>M. Åsell, "Development of optimized radiation therapy using external electron and photon beams," Ph.D. Thesis, University of Stockholm, 1999.
- <sup>17</sup>T. R. Mackie, P. Reckwerdt, and N. Papanikolaou, "3-D Photon Beam Dose Algorithms," in *3-D Radiation Treatment Planning and Conformal Therapy Volume*, edited by, J. A. Purdy, and B. Emami, (Medical Physics Publishing Corporation, Madison, Wisconsin, 1995) pp.
- <sup>18</sup>D. J. Dawson, "Percentage depth doses for high energy x-rays," *Phys Med Biol* **21**, 226-235 (1976).
- <sup>19</sup>M. S. Patterson, and P. C. Shragge, "Characteristics of an 18 MV photon beam from a Therac 20 Medical Linear Accelerator," *Med Phys* **8**, 312-318 (1981).
- <sup>20</sup>G. Luxton, and M. A. Astrahan, "Output factor constituents of a high-energy photon beam," *Med Phys* **15**, 88-91 (1988).
- <sup>21</sup>Y. Yang, L. Xing, A. L. Boyer, Y. Song, and Y. Hu, "A three-source model for the calculation of head scatter factors," *Med Phys* **29**, 2024-2033 (2002).

- <sup>22</sup>P. B. Dunscombe, and J. M. Nieminen, "On the field-size dependence of relative output from a linear accelerator," *Med Phys* **19**, 1441-1444 (1992).
- <sup>23</sup>R. Mohan, C. Chui, and L. Lidofsky, "Energy and angular distributions of photons from medical linear accelerators," *Med Phys* **12**, 592-597 (1985).
- <sup>24</sup>E. L. Chaney, T. J. Cullip, and T. A. Gabriel, "A Monte Carlo study of accelerator head scatter," *Med Phys* **21**, 1383-1390 (1994).
- <sup>25</sup>A. R. Hounsell, and J. M. Wilkinson, "Tissue standard ratios for irregularly shaped radiotherapy fields," *BJR* **63**, 629-634 (1990).
- <sup>26</sup>T. C. Zhu, B. E. Bjärngard, Y. Xiao, and M. Bieda, "Output ratio in air for MLC shaped irregular fields," *Med Phys* **48**, in press (2004).
- <sup>27</sup>H. H. Liu, T. R. Mackie, and E. C. McCullough, "A dual source photon beam model used in convolution/superposition dose calculations for clinical megavoltage x-ray beams," *Med Phys* **24**, 1960-1974 (1997).
- <sup>28</sup>T. C. Zhu, and B. E. Bjärngard, "Head-scatter off-axis for megavoltage X-rays," *Med Phys* **30**, 533-543 (2003).
- <sup>29</sup>R. Shih, X. A. Li, J. C. H. Chu, and W. L. Hsu, "Calculation of head-scatter factors at isocenter or at center of field for any arbitrary jaw setting," *Medical Physics* **26**, 506-511 (1999).
- <sup>30</sup>A. P. Butler, and J. P. Turner, "Off-axis output factors for 6 MV and 18 MV photons," *Australasian Physics and Engineering Science in Medicine* **20**, 177-182 (1997).
- <sup>31</sup>A. Ahnesjö, S. M., and T. A., "A pencil beam model for photon dose calculation," *Med Phys* **19**, 263-273 (1992).
- <sup>32</sup>T. C. Zhu, B. E. Bjärngard, M. Bieda, Y. Xiao, and K. Fallon, "Should the output factor in-air vary with off-axis Positions?," *Med Phys* **48**, 1831 (2004).
- <sup>33</sup>M. Tatcher, and B. E. Bjärngard, "Head-scatter factors in rectangular fields," *Medical Physics* **20**, 205-206 (1993).
- <sup>34</sup>P. Vadash, and B. E. Bjärngard, "An equivalent-square formula for head-scatter factors," *Med Phys* **20**, 733-734 (1993).
- <sup>35</sup>S. Kim, T. C. Zhu, and J. R. Palta, "An equivalent square formula for determining head scatter factors," *Med Phys* **24**, 1770-1774 (1997).
- <sup>36</sup>T. C. Zhu, B. E. Bjärngard, Y. Xiao, and Y. Yang, "Modelling the output ratio in air for megavoltage photon beams," *Med Phys* **28**, 925-937 (2001).
- <sup>37</sup>M. K. Yu, B. Murray, and R. Slobda, "Parameterization of head-scatter factors for rectangular photon fields using an equivalent square formalism," *Med Phys* **22**, 1329-1332 (1995).
- <sup>38</sup>A. L. McKenzie, and P. H. Stevens, "How is photon head scatter in a linear accelerator related to the concept of a virtual source?," *Phys Med Biol* **38**, 1173-1180 (1993).
- <sup>39</sup>S. Kim, C. R. Liu, C. Chen, and J. R. Palta, "Two-effective-source method for the calculation of in-air output at various source-to-detector distances in wedge fields," *Med Phys* **26**, 949-955 (1999).
- <sup>40</sup>T. C. Zhu, B. E. Bjärngard, and P. Vadash, "Scattered photon from wedges in high-energy x-ray beams," *Med Phys* **22**, 1339-1342 (1995).
- <sup>41</sup>P. H. Huang, L. M. Chin, and B. E. Bjärngard, "Scattered photons produced by beam-modifying filters," *Med Phys* **13**, 57-63 (1986).
- <sup>42</sup>S. J. Thomas, "The effect on wedge factors of scattered radiation from the wedge," *Radiother Oncol* **32**, 271-273 (1994).
- <sup>43</sup>M. K. Islam, and J. Van Dyk, "Effects of scatter generated by beam-modifying absorbers in megavoltage photon beams," *Med Phys* **22**, 2075-2081 (1995).
- <sup>44</sup>H. H. Liu, T. R. Mackie, and E. C. McCullough, "Correcting kernel tilting and hardening in convolution/superposition dose calculations for clinical divergent and polychromatic photon beams," *Med Phys* **24**, 1729-1741 (1997).
- <sup>45</sup>A. E. Schach von Wittenau, P. M. J. Bergstrom, and L. Cox, "Patient-dependent beam-modifier physics in Monte Carlo photon dose calculations," *Med Phys* **27**, 935-947 (2000).
- <sup>46</sup>W. van der Zee, and J. Welleweerd, "A Monte Carlo study on internal wedges using BEAM," *Med Phys* **29**, 876-885 (2002).

- <sup>47</sup>F. Verhaegen, and I. Das, "Monte Carlo modelling of a virtual wedge," *Phys Med Biol* **44**, N251-259 (1999).
- <sup>48</sup>R. Shih, X. A. Li, and J. C. H. Chu, "Dosimetric characteristics of dynamic wedged fields: a Monte Carlo study," *Phys Med Biol* **46**, N281-292 (2001).
- <sup>49</sup>R. Shih, Li, XA, Chu, JCH, "Dynamic wedge versus physical wedge: a Monte Carlo study," *Med Phys* **28**, 612-619 (2001).
- <sup>50</sup>C. M. Ma, Li, JS, Pawlicki, T., Jiang, SB, Deng, J., Lee, MC, Koumrian, T, Luxton, M, Brain, S., "A Monte Carlo dose calculation tool for radiotherapy treatment planning," *Phys Med Biol* **47**, 1671-1689 (2002).
- <sup>51</sup>J. van Dam, A. Bridier, C. Lasselin, N. Blanckaert, and A. Dutreix, "Influence of shielding blocks on the output of photon beams as a function of energy and type of treatment unit," *Radiother Oncol* **24**, 55-59 (1992).
- <sup>52</sup>M. Thatcher, and B. E. Bjärngard, "Head-scatter factors in blocked photon fields," *Radiother Oncol* **33**, 64-67 (1994).
- <sup>53</sup>P. D. Higgins, D. N. Mihailidis, F. M. Kahn, E. J. Lee, and A. S. Ahuja, "Blocked field effects on collimator scatter factors," *Physics in Medicine and Biology* **42**, 2435-2447 (1997).
- <sup>54</sup>M. K. Yu, and R. S. Sloboda, "Effect of beam blocking on linac head scatter factors," *Int J Radiat Oncol Biol Phys* **37**, 465-468 (1997).
- <sup>55</sup>H. Kubo, "Telescopic measurements of backscattered radiation from secondary collimator jaws to a beam monitor chamber using a pair of slits," *Med Phys* **16**, 295-298 (1989).
- <sup>56</sup>C. Duzenli, B. McClean, and C. Field, "Backscatter into the beam monitor chamber: Implications for dosimetry of asymmetric collimators," *Med Phys* **20**, 363-367 (1993).
- <sup>57</sup>K. L. Lam, M. S. Muthuswamy, and R. K. Ten Haken, "Measurement of backscatter to the monitor chamber of medical accelerators using target charge," *Med Phys* **25**, 334-338 (1998).
- <sup>58</sup>M. K. Yu, R. S. Sloboda, and F. Mansour, "Measurement of photon beam backscatter from collimators to the beam monitor chamber using target-current-pulse-counting and telescope techniques," *Phys Med Biol* **41**, 1107-1117 (1996).
- <sup>59</sup>P. H. Huang, J. Chu, and B. E. Bjärngard, "The effect of collimator-backscatter radiation on photon output of linear accelerators," *Med Phys* **14**, 268-269 (1987).
- <sup>60</sup>D. L. Watts, and G. S. Ibbott, "Measurement of beam current and evaluation of scatter production in an 18-MV accelerator," *Med Phys* **14**, 662-664 (1987).
- <sup>61</sup>A. R. Hounsell, "Monitor chamber backscatter for intensity modulated radiation therapy using multileaf collimators," *Physics in Medicine and Biology* **43**, 445-454 (1998).
- <sup>62</sup>H. H. Liu, T. R. Mackie, and E. C. McCullough, "Calculating output factors for photon beam radiotherapy using a convolution/superposition method based on a dual source photon beam model," *Med Phys* **24**, 1975-1985 (1997).
- <sup>63</sup>T. C. Zhu, and B. E. Bjärngard, "The head-scatter factor for small field sizes," *Med Phys* **21**, 65-68 (1994).
- <sup>64</sup>S. Gotoh, M. Ochi, N. Hayashi, S. Matsushima, T. Uchida, S. Obata, K. Minami, K. Hayashi, T. Matsuo, M. Iwanaga, A. Yasunaga, and S. Shibata, "Narrow photon beam dosimetry for linear accelerator radiosurgery," *Radiother Oncol* **41**, 221-224 (1996).
- <sup>65</sup>L. Ma, X. A. Li, and C. X. Yu, "An efficient method of measuring the 4 mm helmet output factor for the Gamma knife," *Physics in Medicine and Biology* **45**, 729-733 (2000).
- <sup>66</sup>J. Spicka, D. Herron, and C. Orton, "Separating output factor into collimator factor and phantom scatter factor for megavoltage photon calculations," *Med Dosim* **13**, 23-4 (1988).
- <sup>67</sup>D. M. Frye, B. R. Paliwal, B. R. Thomadsen, and P. Jursinic, "Intercomparison of normalized head-scatter factor measurement techniques," *Med Phys* **22**, 249-53 (1995).
- <sup>68</sup>P. Jursinic, and B. R. Thomadsen, "Measurements of head-scatter factors with cylindrical build-up caps and columnar miniphantoms," *Med Phys* **26**, 512-517 (1999).
- <sup>69</sup>L. Weber, P. Nilsson, and A. Ahnesjö, "Build-up cap materials for measurement of photon head-scatter factors," *Phys Med Biol* **42**, 1875-86 (1997).
- <sup>70</sup>B. R. Thomadsen, S. Kubsad, B. R. Paliwal, S. Shahabi, and T. R. Mackie, "On the cause of the variation in tissue-maximum ratio values with source-to-detector distance," *Medical Physics* **20**, 723-727 (1993).

- <sup>71</sup>J. Venselarr, S. Heukelom, N. Jager, B. Mijnheer, R. van der Laarse, H. van Gasteren, H. J. van Kleffens, and C. F. Westerman, "Effect of electron contamination on scatter correction factors for photon beam dosimetry," *Medical Physics* **26**, 2099-2106 (1999).
- <sup>72</sup>X. A. Li, M. Soubra, J. Szanto, and L. H. Gerig, "Lateral electron equilibrium and electron contamination in measurements of head-scatter factors using miniphantoms and brass caps," *Med Phys* **22**, 1167-1170 (1995).
- <sup>73</sup>S. Johnsson, C. Ceberg, T. Knöös, and P. Nilsson, "Transmission measurements in air using the ESTRO mini-phantom," *Phys Med Biol* **44**, 2445-2450 (1999).
- <sup>74</sup>M. G. Karlsson, M. Karlsson, R. Sjogren, and H. Svensson, "Semiconductor detectors in output factor measurements," *Radiother Oncol* **42**, 293-296 (1997).
- <sup>75</sup>S. Heukelom, J. H. Lanson, and B. J. Mijnheer, "Differences in wedge factor determination in air using a PMMA mini-phantom or a brass build-up cap," *Med Phys* **24**, 1986-91 (1997).
- <sup>76</sup>P. A. Jursinic, "Clinical implementation of a two-component x-ray source model for calculation of head-scatter factors," *Med Phys* **24**, 2001-2007 (1997).
- <sup>77</sup>A. Ahnesjö, "Collimator scatter in photon therapy beams," *Med Phys* **22**, 267-278 (1995).
- <sup>78</sup>T. C. Zhu, Bjärngard, B. E., Shackford, H., "X-ray source and the output factor," *Med Phys* **22**, 793-798 (1995).
- <sup>79</sup>J. R. Palta, D. K. Yeung, and V. Frouhar, "Dosimetric considerations for a multileaf collimator system," *Med Phys* **23**, 1219-1224 (1996).
- <sup>80</sup>M. J. Day, and G. A. Aird, "The equivalent-field method for dose determinations in rectangular fields," *Br J Radiol (Suppl)* **17**, 105-114 (1983).
- <sup>81</sup>J. Clarkson, "A note on depth dose in fields of irregular shape," *Br J Radiol* **14**, 265-268 (1941).
- <sup>82</sup>A. L. Boyer, T. G. Ochrn, C. E. Nyerick, T. J. Waldron, and C. J. Huntzinger, "Clinical dosimetry for implementation of a multileaf collimator," *Med Phys* **19**, 1255-1261 (1992).

Table 1 Summary of terminology used to describe the output radiation.

Beam component Interactions in patient	Direct particles		Indirect particles (headscatter)			Contaminant charged particles
	Open beam	Collimator leakage	Flattening filter scatter	Collimator scatter	Modulator scatter	
Primary dose	Direct primary dose		Indirect primary dose			–
Scatter dose	Direct scatter dose		Indirect scatter dose			–
Charged particle contamination dose	–		–			Charged particle contamination dose
Total dose	Direct dose		Indirect dose (head scatter dose)			Charged particle dose

Table 2. Parameterization of open, square field from different accelerators. Taken from Zhu *et al.*<sup>36</sup>

Model	Energy (MeV)	$a_1$ (cm <sup>-1</sup> )	$a_2$	$\lambda$ (cm)	Max deviation (%)	Std deviation (%)
Varian 2300CD	6	0.0015	0.064	8.12	0.4	0.3
	15	0.0014	0.050	8.45	0.4	0.2
Varian 2100CS	6	0.0013	0.066	8.74	0.1	0.1
	10	0.0014	0.076	8.47	0.2	0.1
Varian 2100CD/MLC	6	0.0013	0.067	8.06	0.4	0.2
	15	0.0012	0.051	7.47	0.3	0.2
Varian Clinac 1800	6	0.0009	0.072	7.96	0.1	0.1
	18	0.0010	0.074	8.11	0.2	0.1
Varian Clinac 6/100	6	0.0008	0.066	8.47	0.5	0.3
Varian Clinac 600C	6	0.0005	0.053	8.80	0.3	0.2
Elekta SL75/5 #1	6	0.0008	0.059	7.52	0.4	0.2
Elekta SL75/5 #2	6	0.0007	0.061	7.81	0.6	0.4
Elekta SL20	6	0.0005	0.081	9.99	0.6	0.3
	20	0.0008	0.119	8.48	0.3	0.2
Elekta SL25/MLC	6	0.0003	0.069	10.8	0.6	0.4
	25	0.0007	0.104	7.64	0.8	0.5
Elekta SL25	6	0.0007	0.066	9.31	0.4	0.2
	25	0.0007	0.102	7.77	0.6	0.4
Siemens Primus	6	0.0004	0.099	9.15	0.5	0.3
	18	0.0006	0.115	7.95	0.9	0.4
Siemens KD2	6	0.0004	0.079	9.69	0.4	0.2
	15	0.0004	0.088	9.19	0.3	0.2
Siemens MXE	6	0.0005	0.117	8.21	0.8	0.3
Cobalt T-1000	1.25	0.0012	0.086	14.2	0.4	0.2

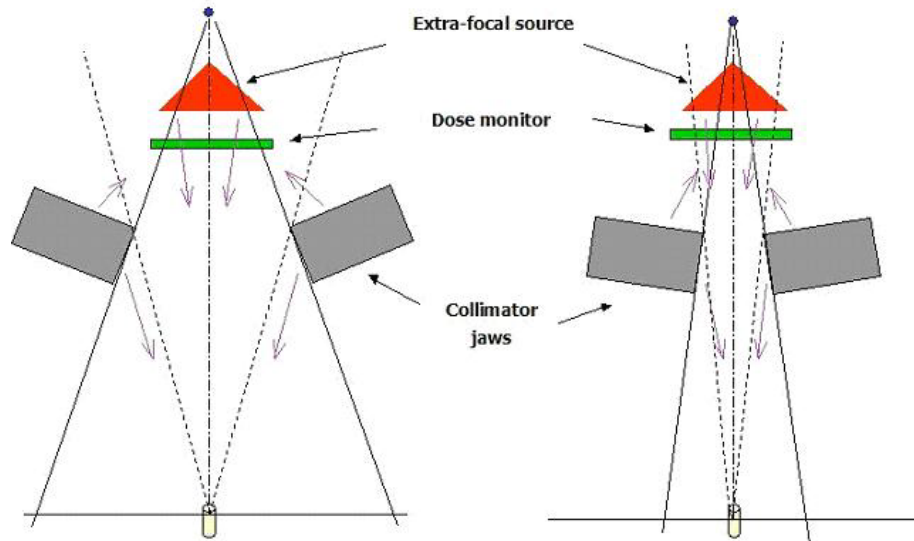


Figure 1 a. The detector's eye view of the scattering sources in the treatment head is the conceptual basis for head scatter modeling.

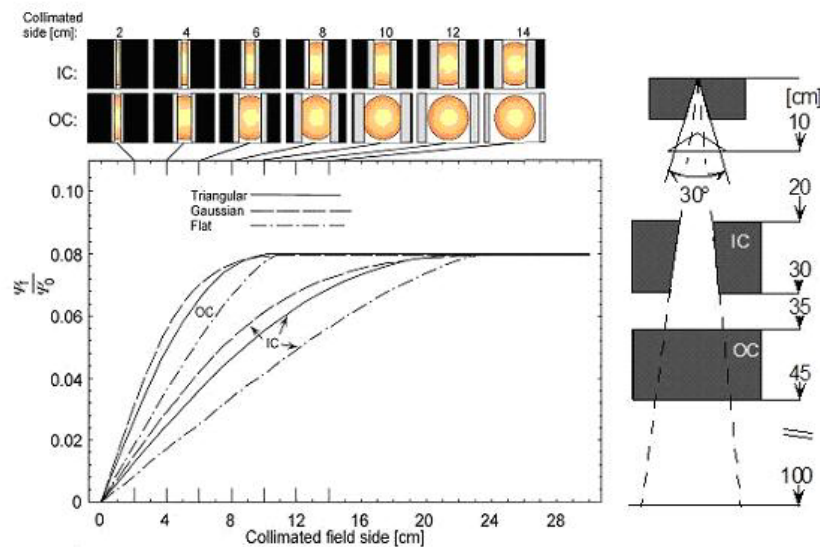


Figure 1b. Flattening filter scatter on the beam axis at a distance of 100 cm for rectangular fields of varying size using the geometry in the right panel. IC and OC mark the curves for which the smallest field side is defined by the inner and outer collimators, respectively. The size of the other side of the field is 40 cm. The treatment head geometry to the right. The panel at the top shows the visible part of the flattening filter for the tick-marked field sizes. Three different source distributions are used, triangular, Gaussian and a constant (flat), all of equal total intensity, 8 % of the direct beam (from Ahnesjö<sup>13</sup>).

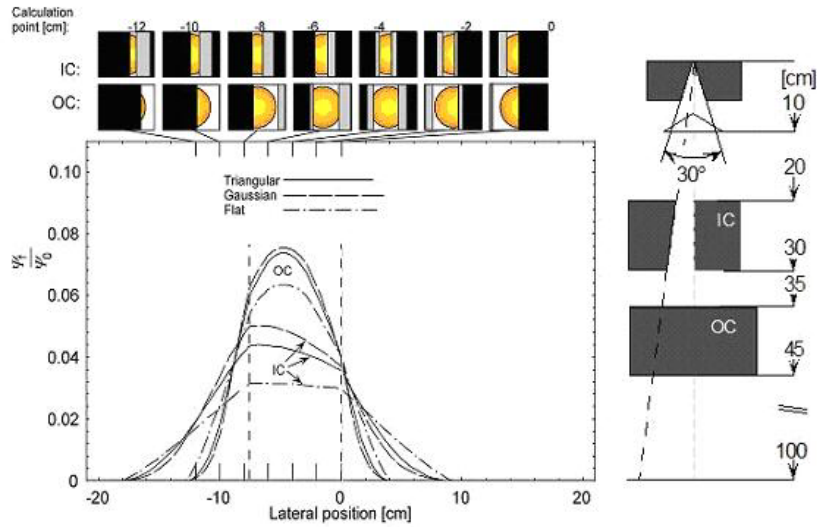


Figure 1c. Flattening filter scatter profiles at the isocenter plane for 7.5x40 cm<sup>2</sup> asymmetric fields where IC and OC mark the curves for which the 7.5 cm side is defined by the inner and outer collimators, respectively. Treatment head geometry to the right. The scatter source is modelled with triangular, flat and Gaussian distributions; all of equal integral intensity corresponding to 8% scatter with unblocked view of the filter at a calculation point 100 cm from the beam source. On top the calculation-point's eye view of the flattening filter for the field defined by inner (upper row) and outer (lower row) collimators are shown for tick-marked positions in the isocenter plane (from Ahnesjö<sup>13</sup>).

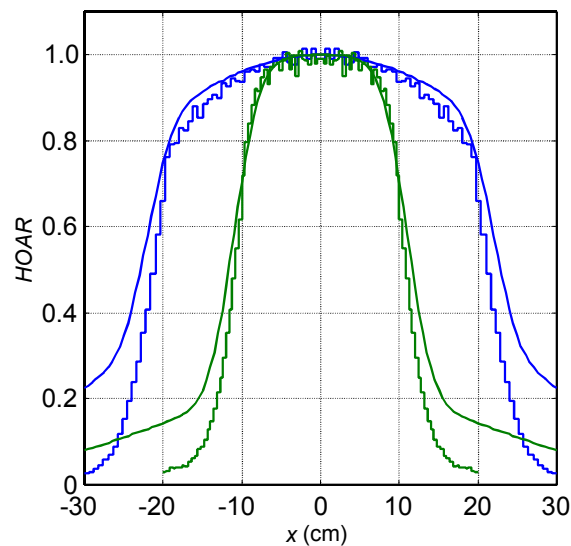


Figure 2. Comparison of *HOAR* between measurements (solid lines) and Monte-Carlo simulation (histogram) for two field sizes: 20 × 20 cm<sup>2</sup> and 40 × 40 cm<sup>2</sup>. All curves are normalized to 1 for  $x = 0$  except for normalization for MC simulations is made for a mean value near  $x = 0$  to reduce statistical error. Taken from Zhu *et al.*<sup>28</sup>

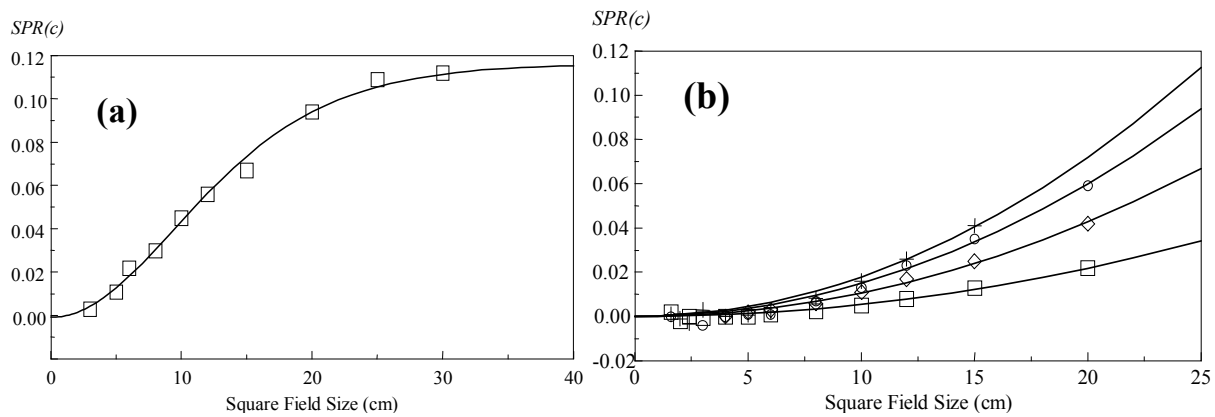


Figure 3. The field size dependence of the ratio of headscatter-to-direct radiations on the central axis for (a) the internal wedge of SL75-5 and (b) the external wedge of a Varian 2100C. Taken from Zhu *et al*<sup>40</sup>

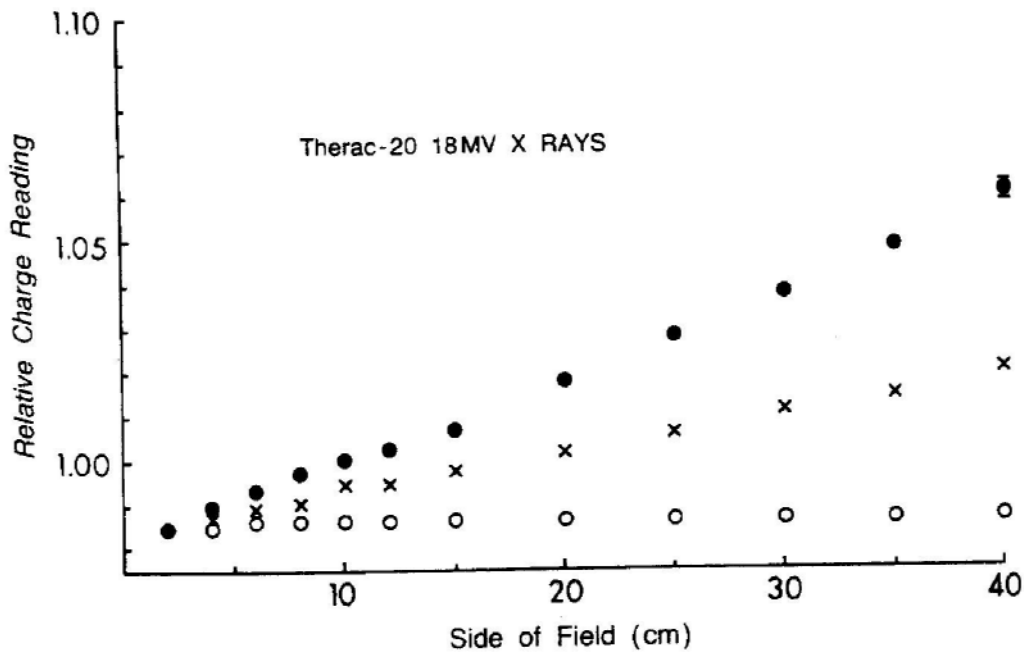


Figure 4. Results of Monitor backscattering obtained by a telescopic method with an 18 MV x-ray from a Therac-20 accelerator. Different symbols represent different collimator settings: • square fields; x fixed inner jaws; o – fixed outer jaws. (Taken from Kubo<sup>55</sup>)

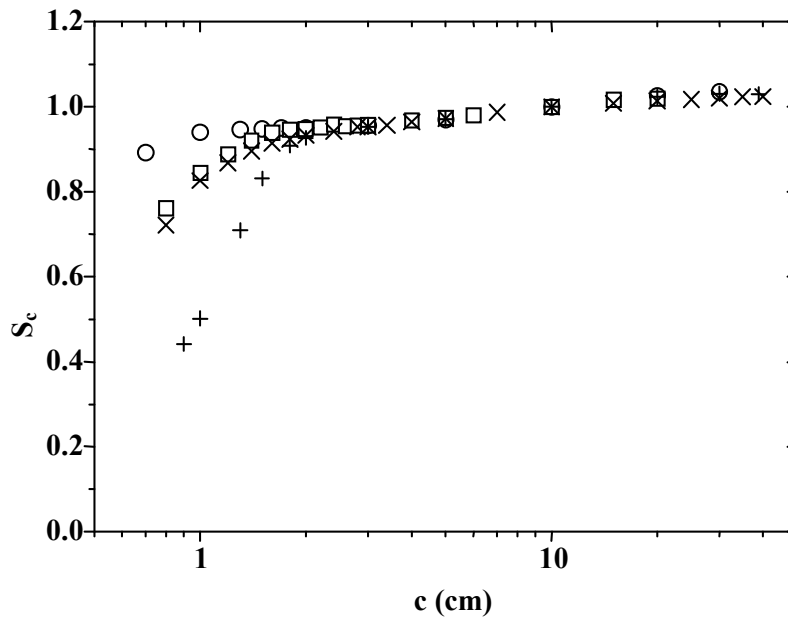


Figure 5.  $S_c$  for open field of four accelerators were shown.  $\circ$  — Varian Clinac 1800, 10 MV,  $\square$  — Philips SL25, 6 MV,  $\times$  — Philips SL75-5, 6 MV,  $+$  — Varian Clinac 6/100, 6 MV. (Taken from Zhu *et al.*<sup>63</sup>)

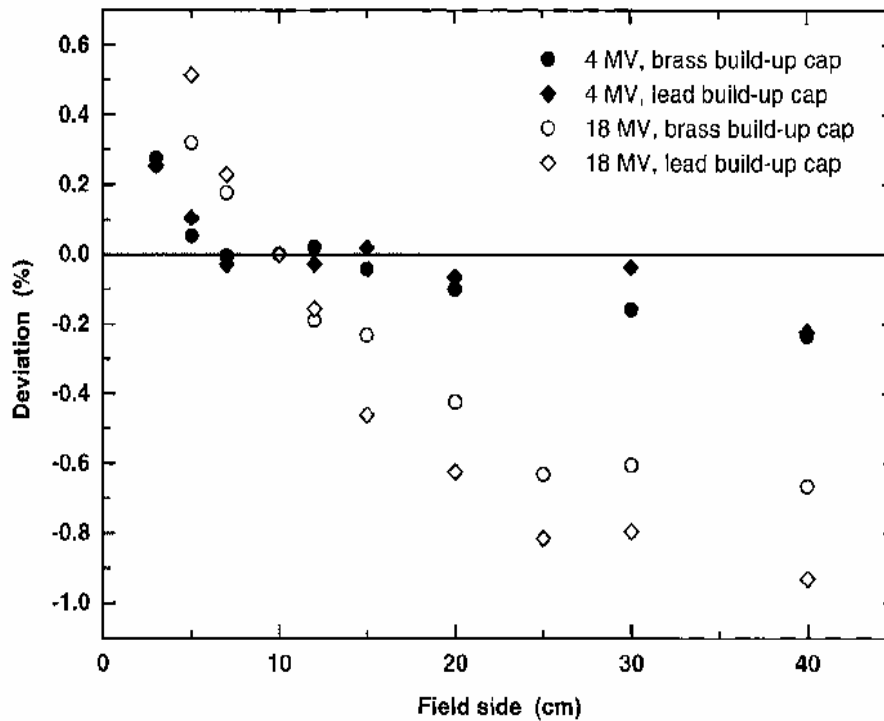


Fig. 6. Deviation in the result of  $S_c$  measurement caused by using high Z material, relative to that using water-equivalent miniphantom. (Taken from Weber *et al.*<sup>69</sup>)



Fig. 7. Recommended miniphantom for measurement of  $S_c$ .

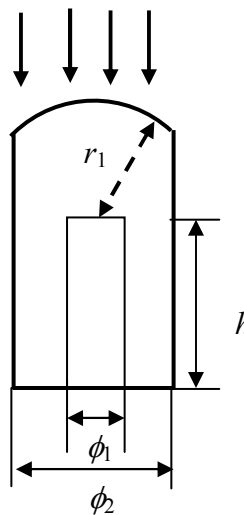


Fig. 8 Schematics of a brass miniphantom recommended for measurements of  $S_c$  for square fields larger than  $1.5 \times 1.5 \text{ cm}^2$ . The longitudinal thickness (or radius of partial-sphere) of the miniphantom facing the radiation should equal to or be larger than 1.1 cm (or  $10 \text{ g/cm}^2$ ,  $\rho = 8.9 \text{ g/cm}^3$ ). The inner diameter of the miniphantom,  $\phi_1$  equals to the outer diameter of the detector, e.g. 0.6 cm. The height,  $h$ , should be sufficient long to cover the detector sensitive volume, e.g., 2 cm. The outer diameter of the miniphantom,  $\phi_2$ , ensures sufficient lateral wall thickness for electron equilibrium,  $\phi_2 = 1.5 \text{ cm}$ .